SOILS AND FOUNDATIONS Vol. 50, No. 2, 227–244, Apr. 2010
Japanese Geotechnical Society

# CENTRIFUGE MODEL TESTS OF A ROCKFILL DAM AND SIMULATION USING CONSOLIDATION ANALYSIS METHOD

YUJI KOHGO[i], AKIRA TAKAHASHI[ii] and TOMOKAZU SUZUKI[iii]

## ABSTRACT

A series of centrifuge model tests for a typical rockfill dam (central core zone type) was conducted in order to investigate behaviour of the dam due to cycles of reservoir water levels. The dam models consisted of comparatively well-compacted core zone and loosely compacted rock zone. A typical result among the model tests was also simulated by using a consolidation analysis method coupled with an elastoplastic model for unsaturated geo-materials. The main behaviour seen from the centrifuge tests was that large amounts of settlements due to wetting within the upstream rock zone were monitored; the crest of the dam at first moved toward upstream and then returned toward downstream in the first reservoir filling; and cracks along the dam axis were observed on the upper parts of the upstream and downstream slopes. A typical result of the dam model tests during reservoir filling was simulated. The simulation results showed that the settlements calculated agreed mostly with those measured; the settlements due to wetting could also be estimated within the upstream rock zone; the horizontal displacements toward upstream increased with the cycles of up-and-down water levels and they concentrated to a shallow region near the upstream surface; tension stresses were calculated at the places where the cracks were monitored in the model tests; and just after construction, arching actions in both the vertical and horizontal effective stress distributions could be seen on both the upstream and downstream boundaries between the core and rock zones but the arching action on the upstream boundary disappeared with water levels going up. The simulation method presented here provided an effective approach to analyze the behaviour of the rockfill dam during reservoir filling periods.

**Key words:** centrifuge model test, constitutive equation, cyclic reservoir water levels, fill dam, numerical analysis, saturated and unsaturated consolidation analysis, saturation collapse (**IGC**: E7/E14/H4)

## INTRODUCTION

Embankment dams are constructed by compacting unsaturated geo-materials (rock and soil materials). After the constructions, the embankments are saturated with reservoir water. Especially, behaviour of embankments due to the first reservoir filling and subsequent cycles of reservoir water levels is hard to estimate, because the following four movements of embankment dams, pointed by Nobari and Duncan (1972), are complexly combined within the behaviour. The four movements and another movement (movement (5)) are illustrated in bold arrows in Fig. 1. Fine arrows shown in Fig. 1 express applied forces. The movements are that (1) the water-load acting on the upstream surface of the impervious core zone causes downstream and downward movements; (2) the water-load acting on the upstream foundation causes upstream and downward movements; (3) the buoyant uplift forces in the upstream shell zone cause upward movements within this zone and downstream rotation of the dam; and (4) collapse of the upstream shell due to wetting causes downward movement within this zone and upstream rotation of the dam. Moreover, (5) deformations due to pore water pressure changes within the impervious core zone may occur. Consolidation analysis methods coupled with elastoplastic models for unsaturated soils are powerful tools to analyze such behaviour. Consolidation analysis methods, which were applied to dams, embankments and slopes, have been well reviewed by Fry et al. (1995) and Kohgo (2003). According to Kohgo's classification of consolidation analysis methods, they were divided into two categories (Methods A and B) on the basis of field equations used. In Method A, force equilibrium equations for whole soil mass and mass conservation equation of pore water are taken into account as field equations under the assumption that pore air pressure is always equal to the atmospheric pressure. In Method B, one more field equation: mass conservation equation of pore air, is added to the field equations used in Method A. In the first stage of applications of these methods to

[i] Associate Professor, Graduate School of Agriculture, Tokyo University of Agriculture and Technology, Tokyo, Japan (kohgo@cc.tuat.ac.jp).
[ii] Tokyo Electric Power Company Limited, Japan.
[iii] Tokyo Electric Power Services Company Limited, Japan.
The manuscript for this paper was received for review on May 13, 2009; approved on January 8, 2010.
Written discussions on this paper should be submitted before November 1, 2010 to the Japanese Geotechnical Society, 4-38-2, Sengoku, Bunkyo-ku, Tokyo 112-0011, Japan. Upon request the closing date may be extended one month.

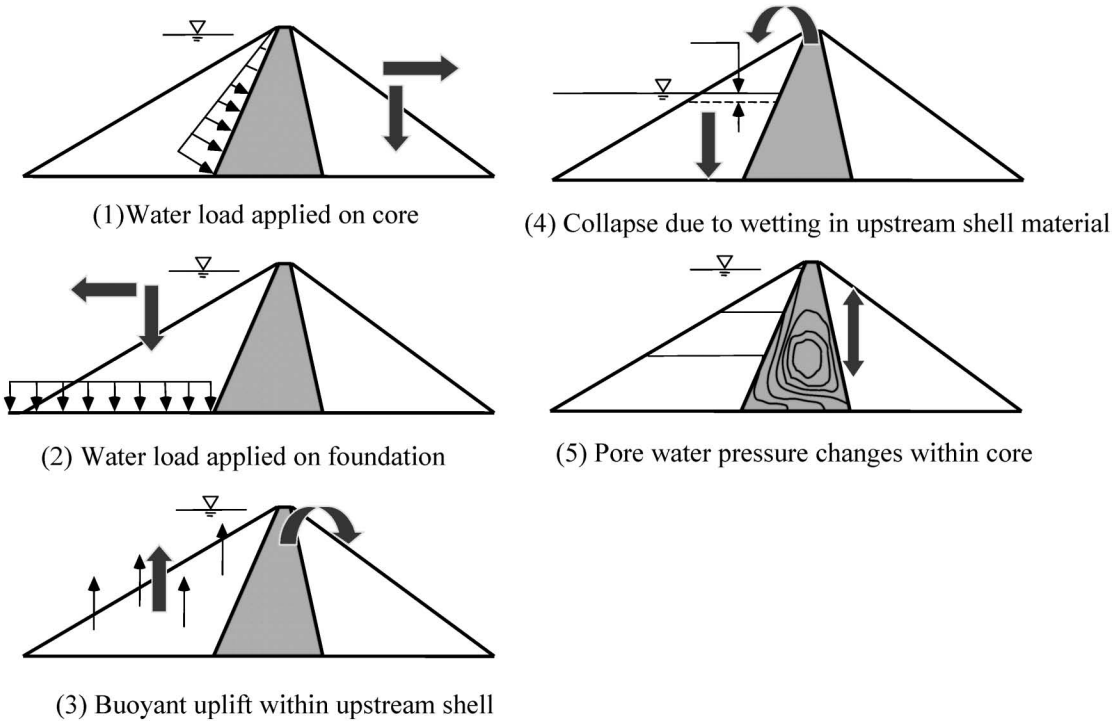


**Fig. 1. Possible movements of rockfill dams during the first reservoir filling**

embankment dams, the analyses are only focused on the estimation of pore water pressures during constructions (Ghaboussi and Kim, 1986; Nakagawa et al., 1985; Laigle et al., 1995; Pagano and Desideri, 1998). The stabilities of embankment dams during constructions were also analyzed (Kohgo and Yamashita, 1988). Subsequently some researchers (Kohgo et al., 2000; Kohgo et al., 2002; Ng and Small, 1999) analyzed embankment dams during construction and first phase of impounding by using the methods. However there are few consolidation analyses by the methods combined with elastoplastic models for unsaturated soils. Moreover no prior research except our research (Kohgo et al., 2006) has focused on investigating the influence of cycles of reservoir water levels on embankment dams.

There are two objectives in this paper. The first is to conduct centrifuge model tests for a rockfill dam model (central core zone type) in order to investigate the behaviour of the dam due to cycles of reservoir water levels. The second is to simulate a typical model test result by using a consolidation analysis method coupled with an elastoplastic model for unsaturated geo-materials.

## CENTRIFUGE TEST

A series of centrifuge model tests were conducted for a rockfill dam model (central core zone type) in order to investigate the behaviour of the rockfill dam during the first reservoir filling and due to cycles of reservoir water levels. As the reliability was confirmed through these tests, we will only mention about the model test simulated here.

**Table 1. Physical properties of core and rock materials**

| Materials | | | Core | Rock |
|---|---|---|---|---|
| Density of soil particle $\rho_s$ (g/cm$^3$) | | | 2.744 | 2.742 |
| Consistency | LL | (%) | 49.1 | — |
| | PL | (%) | 24.2 | — |
| | PI | | 24.9 | — |
| Compaction test (for core 1E$_c$, for Rock 0.5E$_c$) | $\rho_{dmax}$ (Mg/m$^3$) | | 1.764 | 2.154 |
| | $w_{opt}$ (%) | | 18.5 | 8.6 |
| Maximum Particle size (mm) | | | 2.0 | 9.5 |
| Initial water content (%) | | | 24.1 | 1.8 |

## TEST PROCEDURE

The centrifuge model test apparatus used had the loading capacity = about 7 MN and the turning radius = 7.01 m at the bottom of the bucket in which a steel soil box with an inner dimension 190 cm in width, 60 cm in height and 80 cm in depth could be loaded. A dam model was constructed in the soil box using two materials: core and rock. Their physical properties are shown in Table 1. The maximum particle sizes used in the model tests were 2.0 mm for the core and 9.5 mm for the rock. The grading curves are shown in Fig. 2. Teflon sheets were stuck on the sidewalls of the soil box in order to reduce frictions between the embankment model and the sidewalls of the soil box. Steel projections with a 9 mm × 9 mm section were installed on the soil box base in order to increase the frictional resistance between the embankment model and the soil box base. The core and rock materials were compacted by dropping a steel weight of 9.7 kg with a 12.5 cm × 8.0 cm base section from 10 cm height so that dry den-

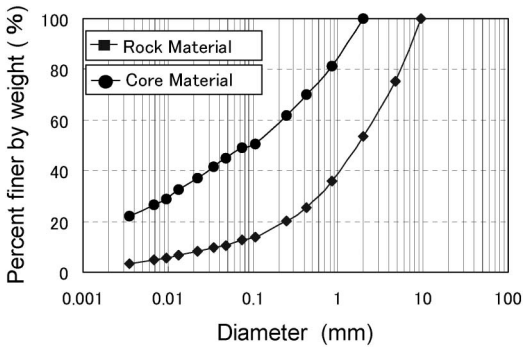


**Fig. 2. Grading curves of core and rock materials used**

**Table 2. Initial conditions of dam model**

| Materials | Core | Rock |
|---|---|---|
| Dry density $\rho_d$ (Mg/m$^3$) | 1.68 | 1.87 |
| Water content (%) | 20.0 | 5.0 |
| D value (%)* | 95.2 | 86.8 |
| Difference from $w_{opt}$ (%) | +1.5 | −3.6 |

* D value = 100 $\rho_d/\rho_{dmax}$ that means degree of compaction.

sities were 1.68 g/cm$^3$ for the core and 1.87 g/cm$^3$ for the rock, respectively. The water contents of the core and rock materials at compaction were 20.0% ($w_{opt}$ + 1.5%, $w_{opt}$: optimum water content at Proctor's energy = 100%) and 5.0% ($w^*_{opt}$ − 3.6%, $w^*_{opt}$: optimum water content at Proctor's energy = 50%), respectively. The spreading thicness of each was 3 cm. The initial values of the degree of saturation after compaction were 86.7% for the core and 29.7% for the rock, respectively. The initial condition of the dam model is summarized in Table 2.

The cross section of the model is shown in Fig. 3. The dimensions of the model used were 40 cm in height, 10 cm in crest width, 80 cm in depth, and 174 cm in base length. It had 1:2.3 upstream and 1:1.8 downstream slopes. The dimensions of the prototype are also denoted within brackets when 80 g acceleration is applied to the model.

Acceleration was gradually increased and reached to 80 g in $t_m$ = 30 minutes ($t_m$ is model time). After reaching 80 g, the value was kept for about $t_m$ = 40 minutes (Consolidation stage) and then reservoir filling was commenced (Reservoir stage). The 80 g acceleration was kept during the reservoir stage. Pore water pressures and displacements were measured during the test. Eleven pore water pressure transducers (PW-01–PW-11), six vertical displacement conventional transducers in which a 30 mm diameter steel plate was attached to each measurement rod (DV-01–DV-06), three laser sensors for vertical displacements (LV-01–LV-03), and two laser sensors for horizontal displacements (LH-01 and LH-02) were used. The DV series displacement sensors may then measure mean vertical displacements within a 2.4 m diameter area in prototype scale. The layout of sensors installed within the embankment is shown in Fig. 4. Water levels of the reservoir were raised up to 35 cm (28 m in prototype scale) and then drawn down to 15 cm (12 m in prototype scale). Two

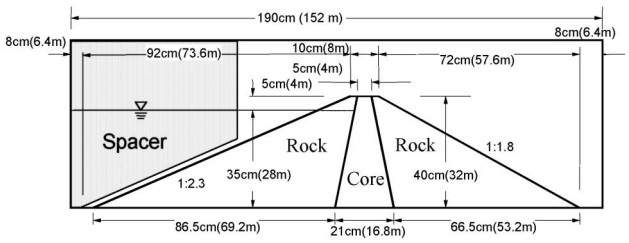


**Fig. 3. The cross section of the dam model**

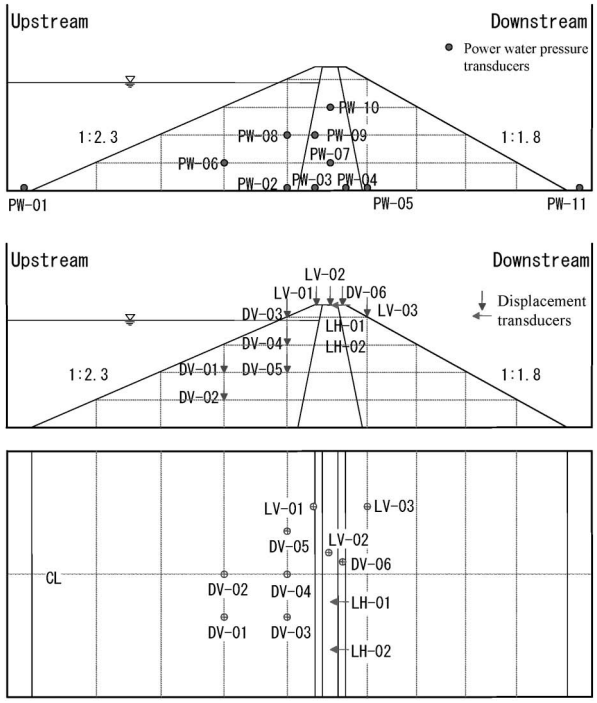


**Fig. 4. Layout of sensors installed within the embankment; (a) layout of pore water transducers in the cross section, (b) Displacement transducers in the cross section, and (c) plane layout**

cycles of rising up and drawing down of the water levels were carried out. As the weight change of the model became as small as possible during application of acceleration, a spacer made of styrene foam was installed into the reservoir (*see* Fig. 3).

## TEST RESULTS

The test results will be described by separating the consolidation and reservoir stages. In displacements, upward and downstream movements express positive. The values of displacements and times are converted to the prototype scale as follows:

$$d_p = N d_m, \tag{1}$$

$$t_p = N^2 t_m, \tag{2}$$

where $d_p$ is prototype displacement, $d_m$ is model displacement, $N$ is acceleration applied, $t_p$ is prototype time, and $t_m$ is model time. All results are described in prototype

scales.

(a) Consolidation stage

Figure 5 shows the relationship between acceleration and elapsed time during the consolidation stage. A $t_p$ of about 200 days was taken for the acceleration to reach a constant value of 80 g. The acceleration was subsequently maintained at 80 g.

Measurement data of vertical and horizontal displacements, and pore water pressures with time are shown in Figs. 6, 7 and 8, respectively. Figure 6 shows the vertical displacements. All the data indicated minus values, that is, settlements and the settlements increased as the acceleration increased. The settlements showed the maximum at the centre of the crest (*see* Fig. 6(e)). The value at the end of this stage was about 0.4 m and the ratio (the maximum settlement during construction/height of embankment) was about 1.3%. The ratio lay within those observed in many existing real dams. As the maximum settlements in the existing dams were normally observed at mid height of the embankments, the deformation pattern of the model test was different from those of the existing dams. The difference was derived from the different procedure of applying self-weights of fills. In real dams, the weights are gradually added with the banking, while the weights were applied at a time in the model test. However both stress distributions are almost the same (Clough and Woodward, 1967).

The settlements measured with all devices at the end of this stage existed within the range from 0.08 m to 0.4 m and the values became greater at the higher and more inner position of the embankment. They became almost constant in about $t_p = 350$ days after starting the test. Comparing Figs. 6(b) and (f), though both the data were

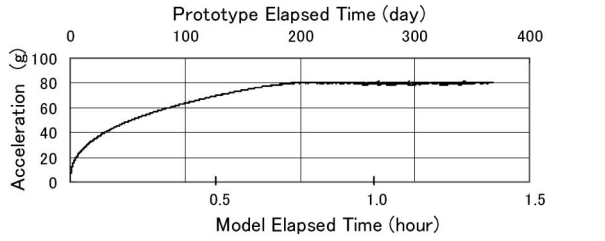


**Fig. 5. Time-acceleration relationship during consolidation stage**

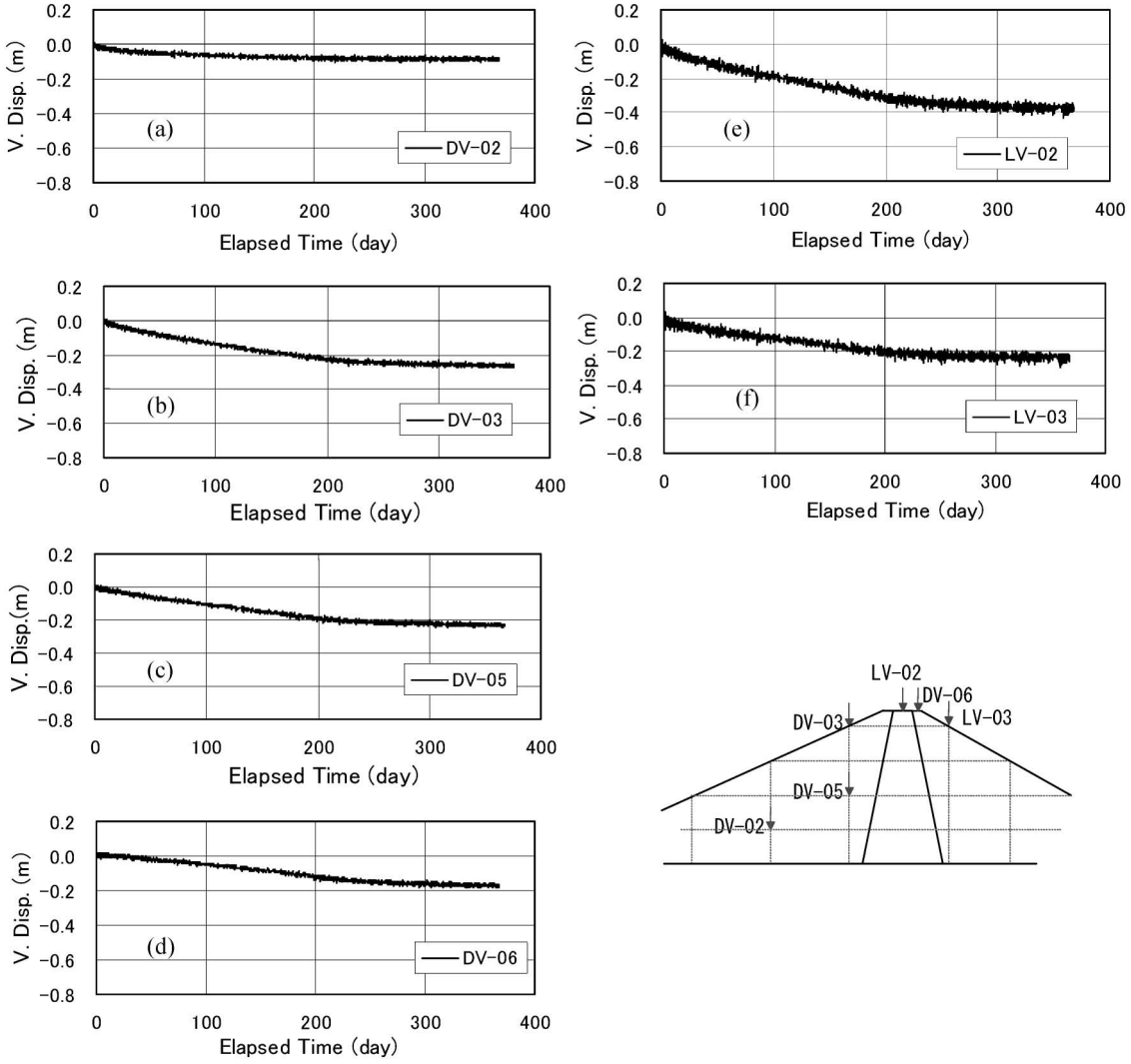


**Fig. 6. Time-vertical displacement relationships during consolidation stage**

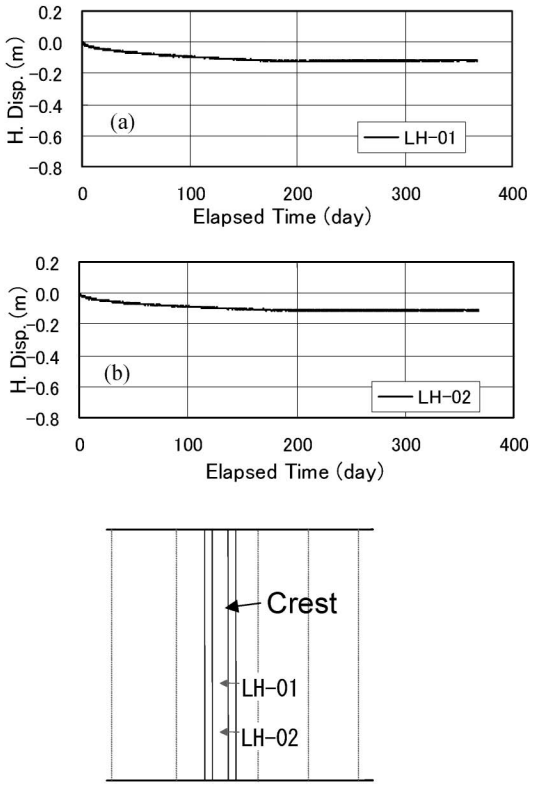


**Fig. 7. Time-horizontal displacement relationships during consolidation stage**

measured at the same height, it was found that the settlements measured on the upstream slope (DV-03) were marginally larger than those done on the downstream slope (LV-03). That might be caused from the difference between the inclinations of the upstream and downstream slopes. As can be seen in Fig. 22(a), the vertical stresses induced in position of DV-03 were greater than that induced in position LV-03.

Figure 7 shows the horizontal displacements measured at the centre of the crest of the embankment (LH-01 and LH-02 devices). The crest moved toward upstream. The horizontal displacements toward upstream increased as the acceleration increased. The behaviour is explained by the settlements on the upstream slope being a little larger than those on the downstream slope (*see* Figs. 6(b) and (f)). The installed position of LH-02 was nearer to the sidewall of the soil box than that of LH-01. As both the behaviour during this stage was almost the same, the effect of sidewall friction seemed to be small in this test. The horizontal displacements became almost constant in about $t_p = 200$ days after starting the test.

Figure 8 shows the pore water pressures measured within the core zone except the data shown in Fig. 8(c). Figure 8(c) shows the data measured on the base within the downstream rock zone. The pore water pressures increased with an increase in acceleration. After the pore water pressures recorded the peaks as shown in Figs. 8(a), (b) and (d), they decreased. The process was consolidation of the core zone. The transducers installed at higher positions (PW-09 and PW-10) and within the rock zone (PW-05) indicated almost null.

(b) Reservoir stage

Figure 9 shows the relationship between acceleration and elapsed time from the commencement of reservoir stage. From the figure it was found that the acceleration value remained constant at 80 g throughout this stage. In this stage, displacements only show values induced during reservoir filling, omitting those induced during the consolidation stage.

Figures 10–13 show the vertical displacements due to cycles of reservoir water levels. Great amounts of settlements were observed during the first reservoir filling at all the measuring points. The settlements must have been caused by saturation collapse. Figures 10 and 11 show the vertical displacements measured along two vertical measurement lines of the embankment. Figure 10 shows the vertical displacements measured at more toe side than Fig. 11. The settlements measured at higher position gave larger values. The water level cycles remarkably affected the vertical displacements measured at the places near the upstream surface. The settlements increased when the water levels went down and decreased when they rose up. The amount of the settlement due to reservoir water fluctuations after the first impounding measured at the inner positions (DV-01, DV-02, and DV-05) were small and most of the settlements occurred during the first impounding. However the amounts measured near upstream surface (DV-03 and DV-04) were relatively large. The behaviour that settlements increased when the water levels went down and decreased when they rose up is reasonable if we take effective stress changes due to the fluctuations of reservoir water into account. This is because effective stresses namely increase when the water level goes down and decrease when it rises up.

Figure 12 shows the vertical displacements measured along a horizontal measurement line of the embankment. The settlements measured with DV-05 were greater than those with DV-01. The settlements measured at more inner part of the embankment seemed to become greater.

Figure 13 shows the vertical displacements measured on the crest of the embankment. The effect of cycles of reservoir water levels on the vertical displacements was smaller than that at other positions already shown in Figs. 10–12. The settlements measured at the most upstream position (LV-01) were the largest and gradually became smaller in order going downstream (*see* LV-02 and LV-06).

Figure 14 shows the horizontal displacements measured on the crest of the embankment. As both the values measured with LH-01 and LH-02 was almost the same, the effect of sidewall friction seemed to be also small during this reservoir stage. The crest moved toward upstream during the first impounding and then returned toward downstream. The crest moved to upstream when the water level went down and moved to downstream when it rose up. It seems to be reasonable that the first behaviour of the crest moving upstream during the first impounding is due to saturation collapses of the upstream rock fill and the following crest moving downstream is induced by

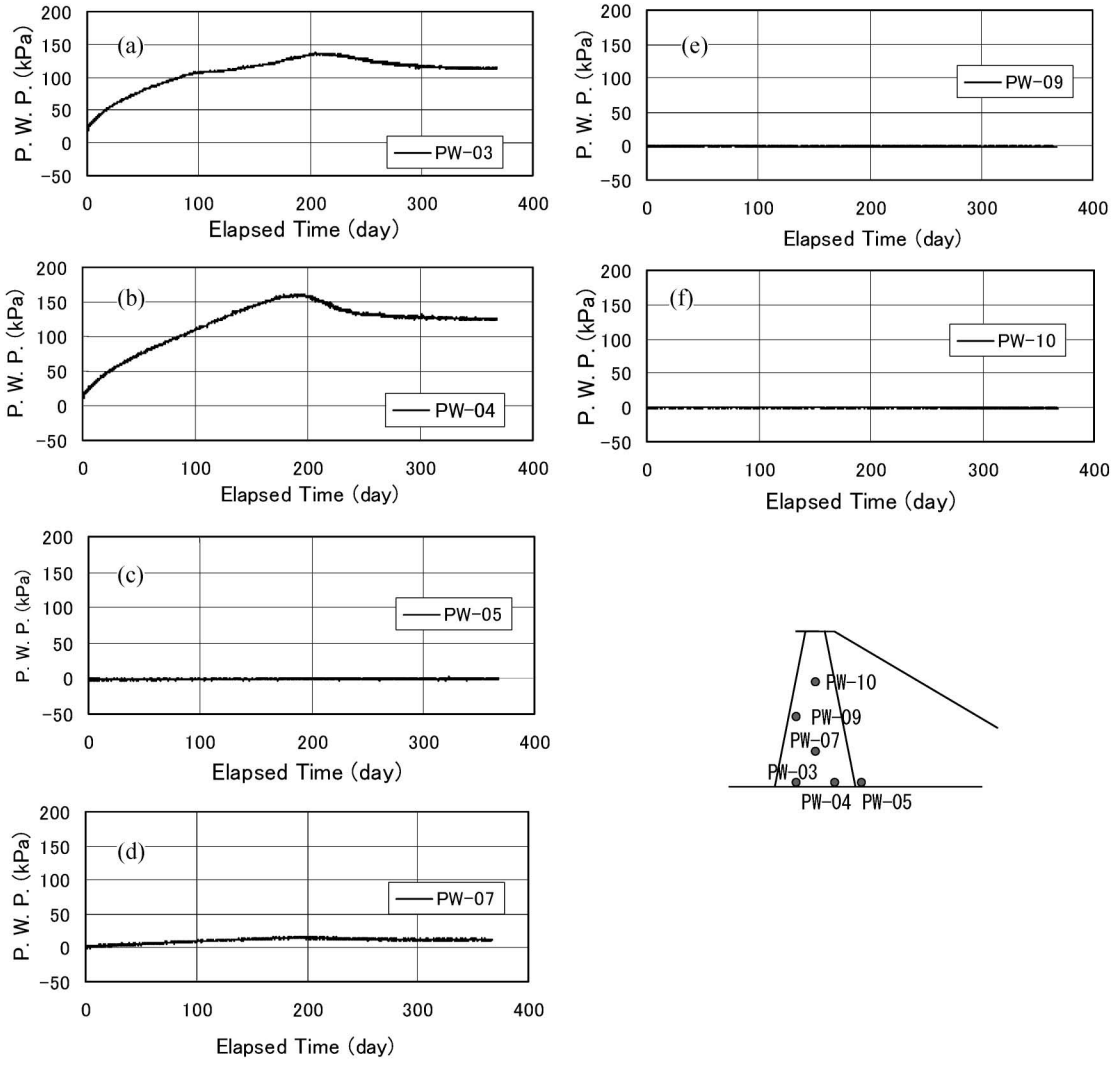


**Fig. 8. Time-pore water pressure relationships during consolidation stage**

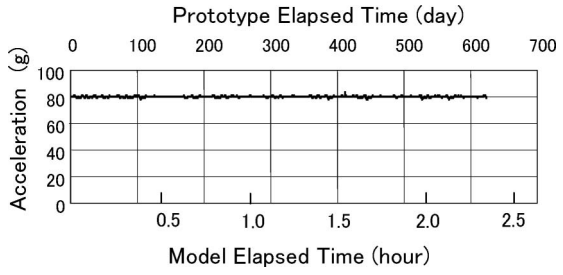


**Fig. 9. Time-acceleration relationship during reservoir stage**

reservoir water pressures. The subsequent behaviour of the crest moving upstream when the water level went down and moving downstream when it rose up may be due to reservoir water pressures.

Figure 15 shows the pore water pressures measured within the core zone. Excess pore water pressures due to banking remained within the core zone just before impounding (*see* the values measured with PW-03 and PW-04). The maximum value was about 120 kPa. The pore water pressures measured with PW-09, which was installed at the most upstream position, quickly responded to the reservoir water levels. The response of the pore water pressures measured with PW-04, which was installed at the most downstream position, to the reservoir water levels was slow.

Photograph 1 illustrates the situations of the dam model after the test. Photos. 1(a), (b) and (c) show the plane view and the views from upstream and downstream of the model, respectively. There were two types of cracks that appeared. One type of the cracks that appeared was on both sides of the crest of the embankment and ran along the dam axis. The other type of cracks only appeared on the core zone and ran across the dam axis. The former must be due to tension forces derived from rotation of the dam toward upstream. The rotation was induced by saturation collapse of the upstream rock fill. This fact is clarified in the analysis described below. The latter might be due to the drying of the core surface.

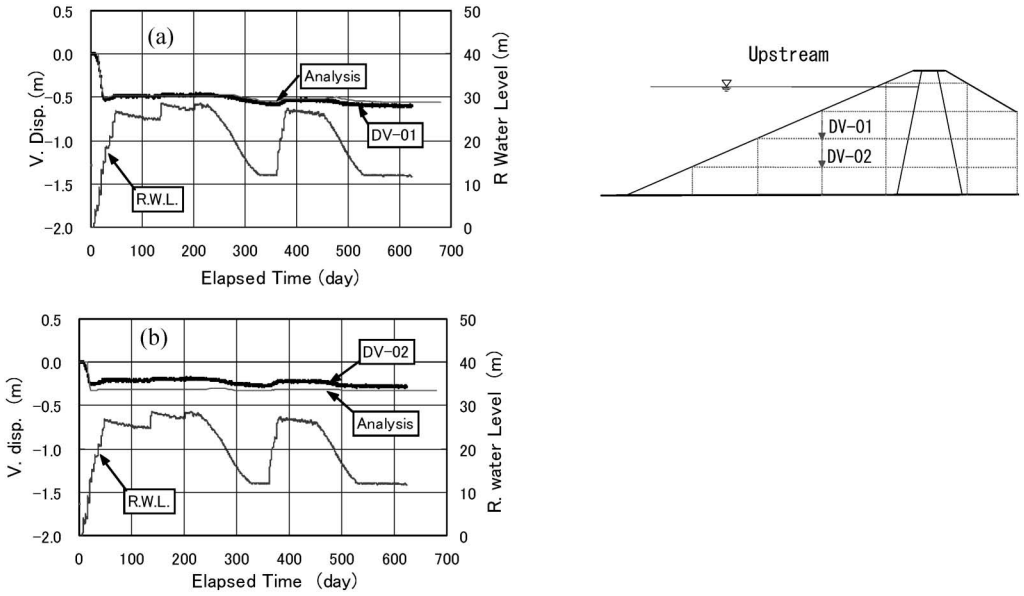


**Fig. 10. Relationship between time and vertical displacements measured with DV-01 and DV-02 devices during reservoir stage (R.W.L. = Reservoir water level)**

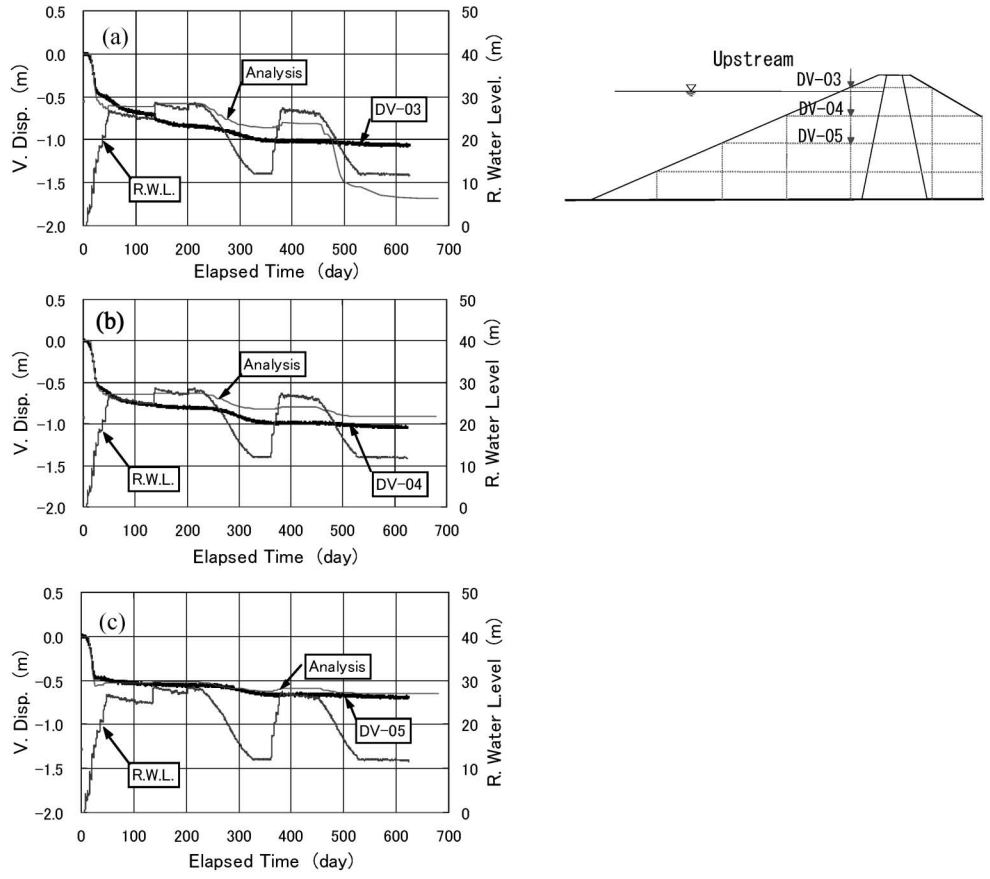


**Fig. 11. Relationship between time and vertical displacements measured with DV-03, DV-04 and DV-05 devices during reservoir stage (R.W.L. = Reservoir water level)**

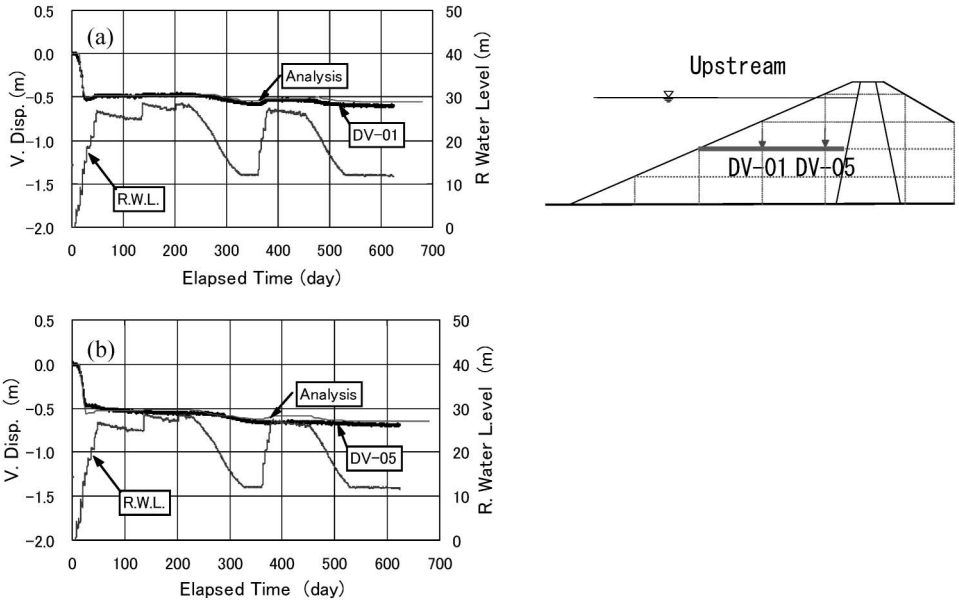


**Fig. 12. Relationship between time and vertical displacements measured along a horizontal measurement line (R.W.L. = Reservoir water level)**

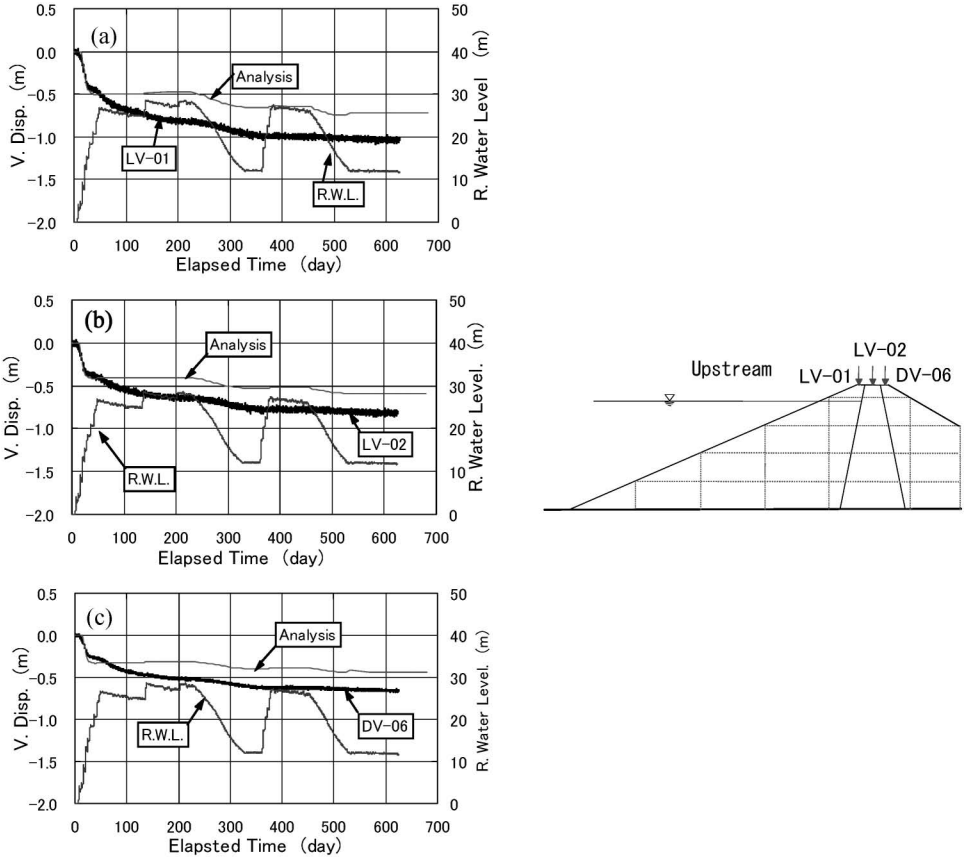


**Fig. 13. Relationship between time-vertical displacements measured on the crest of the embankment during reservoir stage (R.W.L. = Reservoir water level)**

## SIMULATION OF CENTRIFUGE MODEL TEST

### *Analysis Method*

In this section, compression stresses are postulated to be negative. In this simulation, the following two field equations were used. The field equations in weak forms can be represented as:

$$\int_V (\sigma'_{ij,j} + \delta_{ij} u_{eq,j} + \gamma F_i) \cdot \delta u_i^* dV = 0 \tag{3}$$

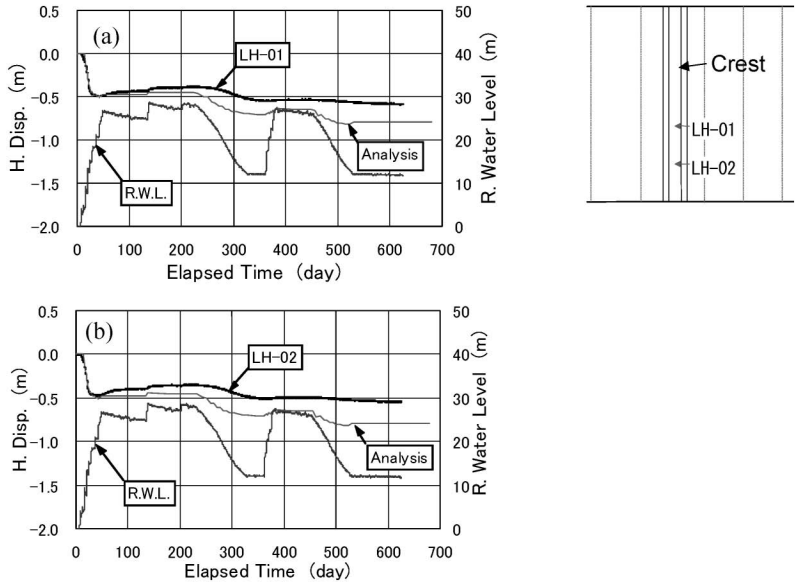


**Fig. 14. Relationship between time-horizontal displacements measured with LH-01 and LH-02 devices during reservoir stage (R.W.L. = Reservoir water level)**

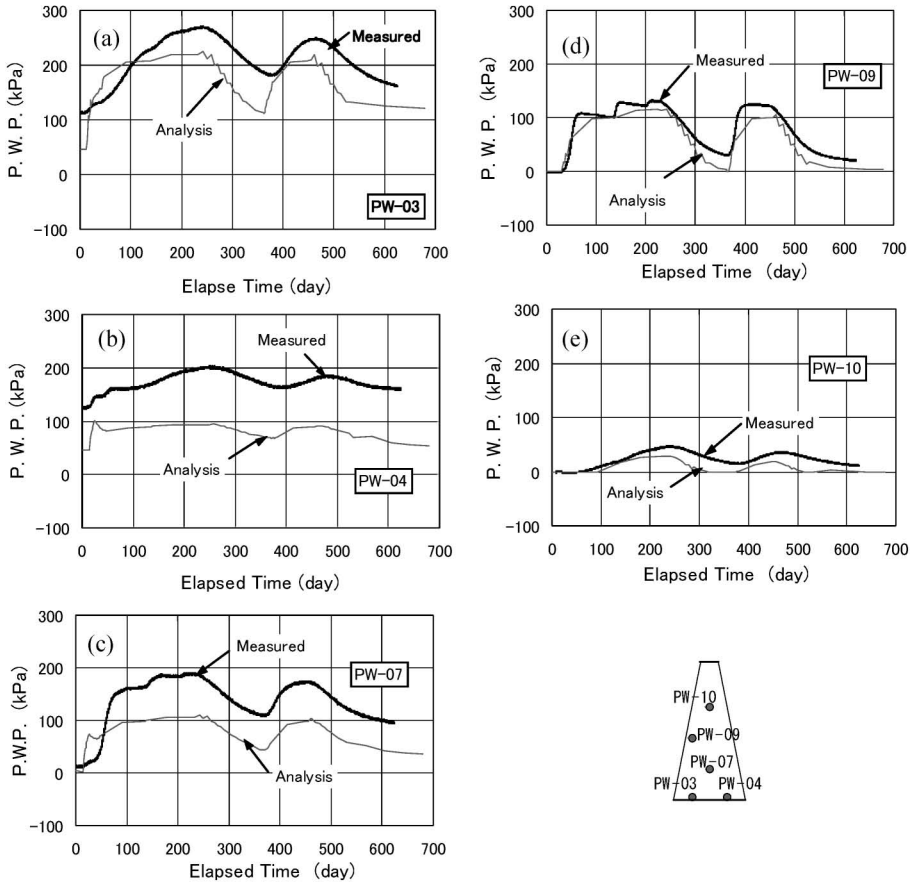


**Fig. 15. Relationship between time-pore water pressures measured within the impervious core zone during reservoir stage**

$$\int_V (q_{i,i} - \dot{a}_{st} + S_r \dot{\varepsilon}_{ii}) \cdot \delta u_w^* dV = 0. \quad (4)$$

Equation (3) is the equilibrium equation of whole soil and Eq. (4) is the Richards' mass conservation equation of pore water. Here, $\sigma'_{ij}$ is effective stress tensor, $\delta_{ij}$ is Kronecker's delta, $u_{eq}$ is equivalent pore pressure, $\gamma$ is unit weight of soil, $F_i$ is components of body force vector, $q_i$ is components of relative displacement velocity vector of water with respect to soil skeleton, $a_{st}$ is change of

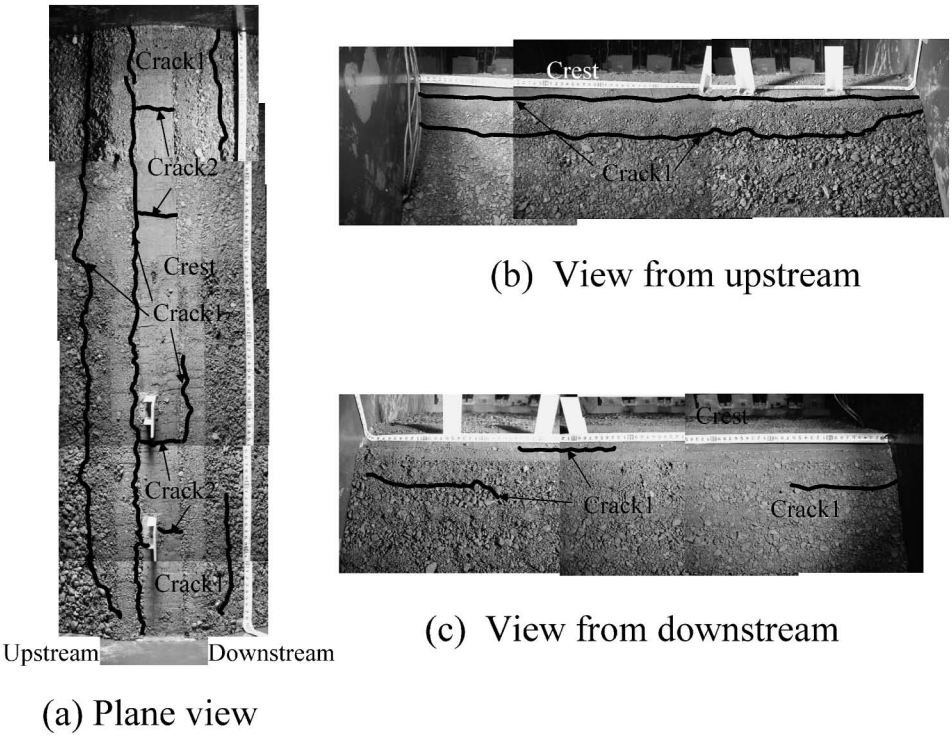


**Photo. 1. Situation of the embankment after centrifuge model test**

storage of water due to change of degree of saturation $S_r$, $\varepsilon_{ii}$ is volumetric strain of soil skeleton, $\delta u_i^*$ is increment of virtual displacement vector, $\delta u_w^*$ is increment of virtual pore water pressure and $V$ is region of analysis. Subscripts after a comma denote spatial differentiation. A superposed dot denotes differentiation with respect to time.

Unknown variables in these equations are displacements of soil skeleton and pore water pressures. The field equations are introduced to the discrete system using the finite element method and the solution procedure based on the modified Newton-Raphson method is adopted. The final matrix equations are as follows:

$$\boldsymbol{\delta}_{m+1} = \boldsymbol{\delta}_m + \Delta\boldsymbol{\delta}_{m+1}, \tag{5}$$

$$\Delta\boldsymbol{\delta}_{m+1} = -\boldsymbol{K}_0^{*-1}\boldsymbol{\Phi}_m, \tag{6}$$

$$\Delta\boldsymbol{\delta}_{m+1}^{T} = \langle \Delta\boldsymbol{u}(t_n)_{m+1} \quad \Delta\boldsymbol{u}_w(t_n)_{m+1} \rangle, \tag{7}$$

$$\boldsymbol{\Phi}_m^{T} = \langle \boldsymbol{\Phi}_m^1 \quad \boldsymbol{\Phi}_m^2 \rangle, \tag{8}$$

$$\boldsymbol{K}_0^* = \begin{bmatrix} \boldsymbol{K} & \boldsymbol{L} \\ \boldsymbol{L}^{T} & -\alpha\cdot\Delta t\bar{\boldsymbol{K}} - \boldsymbol{E} \end{bmatrix}, \tag{9}$$

$$\boldsymbol{K} = \sum_{i=1}^{l} \int_V \boldsymbol{B}^{T}\boldsymbol{D}\boldsymbol{B}dV, \tag{10}$$

$$\boldsymbol{L} = \sum_{i=1}^{l} \int_V \boldsymbol{C}^{T}\boldsymbol{N}dV, \tag{11}$$

$$\bar{\boldsymbol{K}} = \sum_{i=1}^{l} \int_V \boldsymbol{B}_w^{T}\boldsymbol{R}\boldsymbol{B}_w/\gamma_w dV, \tag{12}$$

$$\boldsymbol{E} = \sum_{i=1}^{l} \int_V \boldsymbol{N}_w^{T}\boldsymbol{N}_w/E_f' dV, \tag{13}$$

$$\begin{aligned}\boldsymbol{\Phi}_m^1 = {} & \sum_{i=1}^{l} \int_V \boldsymbol{B}^{T}\boldsymbol{\sigma}'(t_n)_m dV + \sum_{i=1}^{l} \int_V \boldsymbol{C}^{T}\boldsymbol{u}_{eq}(t_n)_m dV \\ & - \sum_{i=1}^{l} \int_{S_3} \boldsymbol{N}_b^{T}\boldsymbol{N}_b\boldsymbol{T}_b(t_n)dS - \sum_{i=1}^{l} \int_V \gamma\boldsymbol{N}^{T}\boldsymbol{F}(t_n)dV, \end{aligned} \tag{14}$$

$$\begin{aligned}\boldsymbol{\Phi}_m^2 = {} & \sum_{i=1}^{l} \int_V S_r\boldsymbol{N}_w^{T}\boldsymbol{C}\boldsymbol{u}(t_n)_m dV - \sum_{i=1}^{l} \int_V S_r\boldsymbol{N}_w^{T}\boldsymbol{C}\boldsymbol{u}(t_{n-1})dV \\ & - \sum_{i=1}^{l} \int_V \boldsymbol{N}_w^{T}\boldsymbol{a}_{st}(t_n)_m dV + \sum_{i=1}^{l} \int_V \boldsymbol{N}_w^{T}\boldsymbol{a}_{st}(t_{n-1})dV \\ & + \alpha\cdot\Delta t \sum_{i=1}^{l} \int_{S_3} \boldsymbol{N}_{wb}^{T}\boldsymbol{N}_{wb}\boldsymbol{Q}_b(t_n)dS \\ & + (1-\alpha)\cdot\Delta t \sum_{i=1}^{l} \int_{S_3} \boldsymbol{N}_{wb}^{T}\boldsymbol{N}_{wb}\boldsymbol{Q}_b(t_{n-1})dS \\ & - \alpha\cdot\Delta t \sum_{i=1}^{l} \int_V \boldsymbol{B}_w^{T}\{\boldsymbol{q}_p(t_n)_m + \boldsymbol{q}_g(t_n)_m\}dV \\ & - (1-\alpha)\cdot\Delta t \sum_{i=1}^{l} \int_V \boldsymbol{B}_w^{T}\{\boldsymbol{q}_p(t_{n-1}) + \boldsymbol{q}_g(t_{n-1})\}dV \end{aligned} \tag{15}$$

where $\sigma'$ is effective stress vector, $\boldsymbol{u}$ is nodal displacement vector, $\Delta\boldsymbol{u}$ is increment of nodal displacement vector, $\boldsymbol{u}_{eq}$ is equivalent pore pressures, $\Delta\boldsymbol{u}_w$ is increment of nodal pore water pressures, $\boldsymbol{a}_{st}$ is change of storage of water due to change of degree of saturation, $\boldsymbol{D}$ is elastic matrix, $\boldsymbol{R}$ is permeability matrix, $\boldsymbol{N}$ is interpolation function for displacement, $\boldsymbol{N}_w$ is interpolation function for pore water pressure, $\boldsymbol{B}$ is nodal displacement-strain matrix, $\boldsymbol{B}_w$ is gradient matrix for pore water pressure, $\boldsymbol{C}$ is nodal displacement-volumetric strain matrix, $\boldsymbol{F}$ is body force vector, $\boldsymbol{T}_b$ is prescribed traction vector on the boundary nodal points, $\boldsymbol{Q}_b$ is prescribed flux vector on the boundary

nodal points, $\boldsymbol{q}$ is flux vector, $E'_f = E_f/n$ ($E_f = \partial S_r/\partial s$, $s$: suction, $n$: porosity), $\alpha$ is coefficient characterizing single-step temporal discretization, $t$ is time, $\Delta t$ is increment of time and $S$ is area of boundary surface. Superscript T denotes transposition of matrix and subscripts b, p, g, m and n denote values on the boundaries, values due to pore water pressure, values due to gravitational potential, number of iterations and number of time steps, respectively. $\Sigma$ denotes summing up with respect to whole elements.

Material nonlinear properties need to be taken into account to conduct consolidation analyses. We considered nonlinear properties of stress-strain relationship, permeability and soil water retention curves. We adopted an elastoplastic model with two suction effects as stress-strain relationship (Kohgo et al., 1993b, 2007). The two suction effects are (a) an increase in suction increases effective stresses, and (b) an increase in suction enhances yield stresses and affects the resistance to plastic deformations. The effective stress equations can be illustrated as in Eqs. (16) to (18).

$$\sigma'_{ij} = \sigma_{ij} - \delta_{ij} u_{eq}, \tag{16}$$

$$u_{eq} = u_a - s \qquad (s \le s_e), \tag{17}$$

$$u_{eq} = u_a - \left[ s_e + \frac{a_e}{s^* + a_e} s^* \right] \qquad (s > s_e), \tag{18}$$

where $\sigma_{ij}$ is total stress tensor and $a_e$ a material parameter. Suction $s$ and effective suction $s^*$ are defined as follows:

$$s = u_a - u_w, \tag{19}$$

$$s^* = \langle s - s_e \rangle. \tag{20}$$

Where $u_a$ is pore air pressure, $u_w$ is pore water pressure, $s_e$ is air entry suction and the brackets $\langle\ \rangle$ denote the operation $\langle z \rangle = 0$ at $z < 0$ and $\langle z \rangle = z$ at $z \ge 0$.

The suction effect (b) may be formulated by evaluating the state surface, which defines elastoplastic volume change behaviour in unsaturated soils (Kohgo et al., 1993a). The state surface can be plotted in the space with the axes: mean effective stress $p'$, effective suction $s^*$, and void ratio $e$. The shapes of state surfaces depend on the types of soils. Here, they are assumed to be expressed as Eqs. (21)–(23) when $s^*_m = \infty$.

$$e = -\lambda^* \log(-p') + \Gamma^*, \tag{21}$$

$$\lambda^* = \lambda + \frac{\lambda^*_{f1} s^*}{s^* + a^*_f}, \tag{22}$$

$$\Gamma^* = e^0_{01} + \frac{(\Gamma - e^0_{01})\lambda^*}{\lambda}, \tag{23}$$

where $\lambda = \lambda^*$ in saturation, $\Gamma = \Gamma^*$ in saturation, $\lambda^*$ is slopes of $e - \log(-p')$ curves in the elastoplastic range, $\Gamma^*$ is void ratios of $e - \log(-p')$ curves in the elastoplastic range at $p' =$ unit, $s^*_m$, $\lambda^*_{f1}$, $a^*_f$, $e^0_{10}$ are material parameters. More details can be found in the reference (Kohgo et al., 2007).

Soil water retention curves are modelled by the Tangential model (Kohgo, 2008). The details can be seen in the reference.

The permeability is considerably influenced by deformations and changes of the degree of saturation of soil. Therefore, the permeability property was assumed to be a function of void ratio $e$ and degree of saturation $S_r$ as follows.

$$k = k_s \cdot E_p \cdot H_p, \tag{24}$$

$$E_p = \frac{1 + e_0}{1 + e} \left( \frac{e}{e_0} \right)^{n_p}, \tag{25}$$

$$H_p = \left( \frac{S_r - S_{rf}}{S_{re} - S_{rf}} \right)^{m_p}. \tag{26}$$

Where $k_s$ is the permeability at saturation, $S_{re}$ is degree of saturation at air entry, $S_{rf}$ is degree of saturation at the point with the lowest suction among the points where the tangential slope of soil water retention curve is almost constant in the range of greater suction (Kohgo, 2008), $e_0$ is initial void ratio and $m_p$ and $n_p$ are material parameters.

In the elastic range, the elastic moduli were assumed to be functions of $p'$ and $J_2$ as follows:

$$K = \frac{-2.3(1 + e_0)}{\kappa} p' + K_i \tag{27}$$

$$G = G_i + \gamma_J \sqrt{J_2} - \gamma_p p' \tag{28}$$

Where $K$ is bulk modulus, $G$ is shear modulus, and $K_i$, $G_i$, $\gamma_J$ and $\gamma_p$ are material parameters.

*Identification of Parameters and Simulation of Laboratory Tests*

Parameters identified are shown in Table 3. These parameters were identified from isotropic compression, triaxial compression and soil water retention tests. The details of plastic and soil water retention parameters can be seen in the references (Kohgo et al., 2007; Kohgo, 2008). The details of the identification method of the parameters with respect to effective stress and state surface can be seen in the reference (Kohgo et al., 1995).

The simulations of element tests: soil water retention, isotropic compression, and triaxial compression tests, using parameters shown in Table 3 are shown in Figs. 16–18. Figure 16 shows simulation results of soil water retention curves of core and rock materials. In these figures, closed circles and solid lines express experimental and simulation results, respectively. Almost good agreements for both materials were obtained.

Figure 17 shows simulation results of isotropic compression tests for core and rock materials with constant suction values: $s = 0$ and 100 kPa. These simulations were conducted by the FEM saturated and unsaturated consolidation analysis method described above. The right and upper quarter of the specimens was selected for the analyses. Axial symmetric problems were set. In order to satisfy constant suction values, the prescribed suction values were set at all nodal points used to evaluate pore water pressures. In these figures, symbols and lines express experimental and simulation results, respectively. In both materials and suction values, simulation results

**Table 3. Material parameters used in simulation**

| | Elastoplastic | | | | | | | |
|---|---|---|---|---|---|---|---|---|
| | $\kappa$ | $K_i$ (kPa) | $G_i$ (kPa) | $\gamma_J$ | $\gamma_p$ | $\phi'$ | $\phi\phi'_{cs}$ | $R$ |
| Core | 0.013 | $8.3\times10^3$ | $3.4\times10^3$ | −146.3 | 107.6 | 31.7 | 38.7 | 0.5 |
| Rock fill | 0.009 | $3.6\times10^3$ | $1.4\times10^3$ | −193.0 | 138.6 | 31.0 | 36.8 | 0.5 |

| | State surface | | | | | Initial condition | | |
|---|---|---|---|---|---|---|---|---|
| | $\lambda$ | $\Gamma$ | $a_1^*$ | $\lambda_{f1}^*$ | $e_{01}^0$ | $e_0$ | $S_{r0}$ | $\rho_{t0}$ (kN/m$^3$) |
| Core | 0.272 | 1.180 | 22.1 | −0.177 | 0.595 | 0.586 | 0.937 | 20.4 |
| Rock fill | 0.120 | 0.621 | 2.56 | 0.029 | 0.047 | 0.414 | 0.314 | 19.4 |

| | Effective stress | | Subloading | Permeability | | |
|---|---|---|---|---|---|---|
| | $a_e$ (kPa) | $s_e$ (kPa) | $\alpha_h$ | $k_s$ (m/day) | $n_p$ | $\lambda_s$ |
| Core | 204.8 | 0.0 | $5.0\times10^5$ | $2.6\times10^{-3}$ | 8.0 | 3.0 |
| Rock fill | 73.3 | 0.0 | $5.0\times10^5$ | $8.6\times10^1$ | 3.0 | 3.0 |

| | Soil water retention | | | | | | |
|---|---|---|---|---|---|---|---|
| | $S_{re}$ | $s_m$ (kPa) | $S_{rm}$ | $c_m$ | $s_f$ (kPa) | $S_{rf}$ | $c_f$ |
| Core | 0.98 | 0.1 | 0.75 | $6.0\times10^{-3}$ | 1500 | 0.25 | $2.5\times10^{-4}$ |
| Rock fill | 0.95 | 5.0 | 0.50 | $3.8\times10^{-2}$ | 1000 | 0.20 | $1.0\times10^{-4}$ |

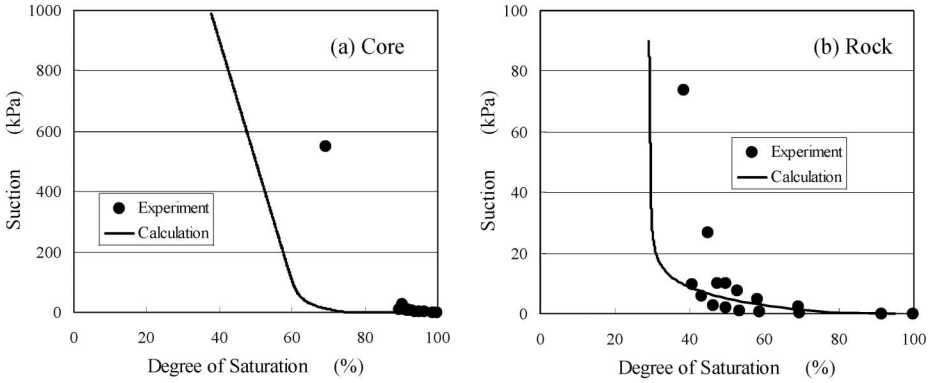


**Fig. 16. Simulation results of soil water retention tests of core and rock materials**

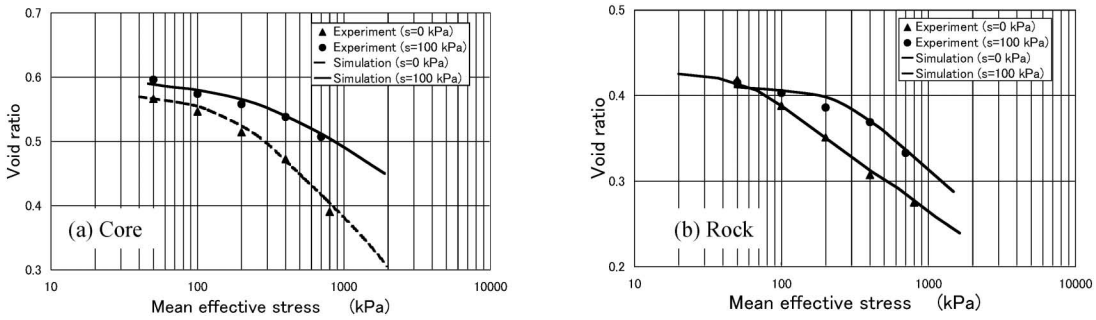


**Fig. 17. Simulation results of isotropic consolidation tests of core and rock materials**

gave good agreements to the experimental ones.

Figure 18 shows simulation results of triaxial compression tests. Triaxial compression tests with a constant suction value: $s=100$ kPa for the core and rock materials were simulated by the FEM saturated and unsaturated consolidation analysis. The simulation region is the same as that in isotropic compression tests, that is, the right and upper quarter of the specimens. Axial symmetric problems were set. For unsaturated specimens, seepage condition (suction is greater than or equal to 0) was satisfied on the upper surfaces of the specimens and undrained condition was postulated on both sides of specimens dur-

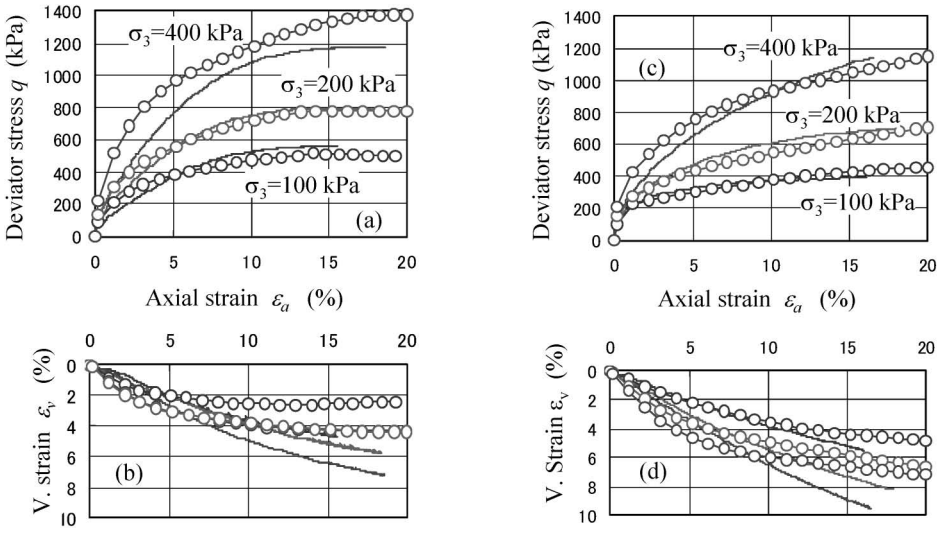


**Fig. 18. Simulation results of triaxial compression tests under a constant suction value $s = 100$ kPa: (a) Deviator stress-axial strain relationship for core material, (b) Volumetric strain-axial strain relationship for core material, (c) Deviator stress-axial strain relationship for rock material, and (d) Volumetric strain-axial strain relationship for rock material**

ing the consolidation processes. Before the shear processes, the prescribed suction values were set at all nodal points used to evaluate pore water pressures. Figures 18(a) and (b) show the simulation results of the core and (c) and (d) for rock materials, respectively. Symbols with lines and solid lines are simulation and experimental results, respectively. The stress-strain relationships were almost consistent with the experimental ones.

*Analysis Results*

The 8 node iso-parametric elements for displacement field and the super-parametric elements for pore water pressure field were used. The reduced integration ($2 \times 2$ Gauss point integration) was also adopted. The finite element mesh and boundary conditions are shown in Fig. 19. Pore water pressures in the rock zone were assumed to maintain the initial values during construction and the same values as water levels of the reservoir were given in the impounding process. Then water loads should be applied on upstream surface. This treatment is different from that mentioned in Fig. 1. In Fig. 1, the effect of pore water pressures within the upstream rock zone was treated as buoyant uplift forces and water loads were applied on the upstream surface of the impervious core. Thus the consolidation behaviour of the core was only considered in this analysis. The base of the embankment was rigid and impervious. The water level of the reservoir first rose up to 28 m (35 cm for the model) and then drew down to 12 m. The few cycles of rising up and drawing down of water levels were carried out as shown in Fig. 20. In this figure, the fine line expresses the water levels measured with PW-02 pore water pressure transducer and the thick line denotes water levels used in the simulation.

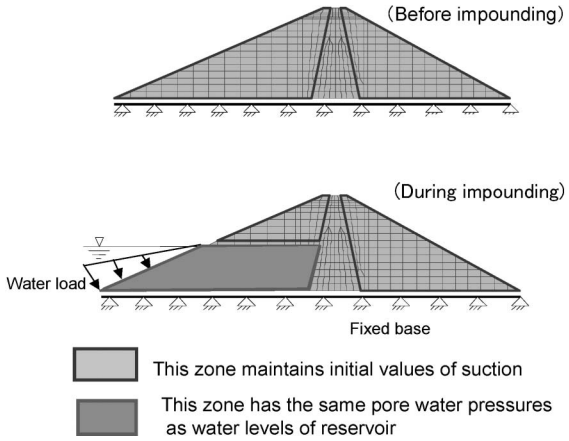


**Fig. 19. FEM mesh and boundary conditions used in simulation**

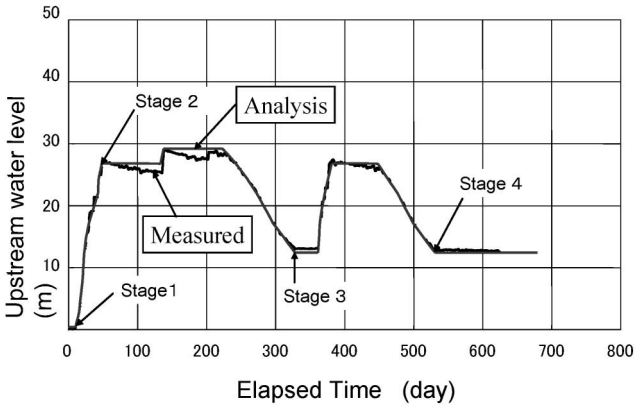


**Fig. 20. Time-reservoir water levels relationship used in simulation**

The comparisons between the vertical and horizontal displacements and the pore water pressures measured and calculated are shown in Figs. 10, 11, 13, 14 and 15. Figures 10, 11 and 13 show the vertical displacements due to reservoir water level cycles. The great amounts of settlements due to saturation collapse can be calculated. It can be seen from Fig. 10 that the vertical displacements

calculated, agreed well with those measured. The settlements increased when the water levels went down and decreased when they rose up. This tendency could also be seen in the results calculated. This behaviour must be caused by effective stress changes due to raising and drawing down reservoir water levels.

Figure 11 is similar to Fig. 10. It was found from Fig. 11(a) that the differences between the settlements measured and calculated expanded during the second drawing down of the water level and a great amount of settlements was calculated. That might be caused by a failure induced within a small area near DV-03 installed place. It was found from Figs. 21(c) and (d) that deformations were concentrated to a thin region near the upstream surface. The settlements measured with DV-04 and DV-05 almost agreed with those calculated.

Figure 13 shows the vertical displacements measured and calculated on the crest of the embankment. The vertical displacements calculated were marginally smaller than those measured. However the change in patterns due to the reservoir water level cycles were similar to those observed, that is, the settlements increased when the water level went down and they decreased when the water levels went up. The affection of reservoir water levels to the settlements was the largest at the most upstream position (*see* LV-01) and became smaller in order moving downstream (*see* LV-02 and DV-06). This tendency was the same in both measured and calculated vertical displacements.

Figure 14 shows the measured and calculated horizontal displacements on the crest of the embankment. The crest moved towards upstream during first reservoir filling and then returned downstream. The crest moved upstream and downstream with decrease and increase in reservoir water levels respectively. The measured trends were almost similar to those calculated. The displacements calculated were marginally larger than those measured.

Figure 15 shows the pore water pressures measured and calculated within the core zone. The amount of excess pore water pressures due to banking measured almost twice larger than those calculated. The agreement in pore water pressures measured and calculated became better as the measurement places became higher at more upstream positions (*see* Figs. 15(a), (d) and (e)).

The distributions of the deformations, the vertical effective stresses, the horizontal effective stresses and the pore water pressures calculated are shown in Figs. 21–24. In the figures, Stages 1–4 are the periods denoted in Fig. 20. Figure 21 shows the deformations of the dam model. The deformations were thrice those calculated in these figures. As the water levels went up, settlements occurred within the upstream rock zone and the embankment rolled toward upstream. Horizontal displacements upstream increased near the upstream slope with the cycles of up-and-down water levels. The horizontal displacements concentrated to a shallow region near the upstream surface but they remained as small values at the deeper places within the upstream rock zone.

Figure 22 shows the distribution of calculated vertical effective stresses. Just after construction (Stage 1), arching actions could be seen on both upstream and downstream boundaries between the core and rock zones and some reductions of vertical effective stresses occurred within the core zone. As the water levels of the reservoir rose, the vertical effective stresses within the upstream rock zone decreased and became smaller than those within the core zone. Following that the arching action on the upstream boundary disappeared. The development and reduction of the vertical effective stresses within the upstream rock zone repeated with up-and-down water levels. The remarkable arching action, which could be seen in Stage 1, never appeared at the upstream boundary. The arching action was derived from the difference between the stiffness of the core and rock materials. The action might then disappear once the rock zone was submerged.

Figure 23 shows the distributions of the horizontal effective stresses calculated. Just after construction, the distributions expressed almost bilateral symmetry as shown in Fig. 23(a). As water levels of the reservoir rose, the horizontal effective stresses within the upstream rock zone decreased but the situation before the impounding remained within the downstream rock zone. The development and reduction of the horizontal effective stresses within the upstream rock zone also repeated with up-and-down water levels. The development occurred with the water level going down and the reduction occurred with the water levels going up. Tension stresses within an up-

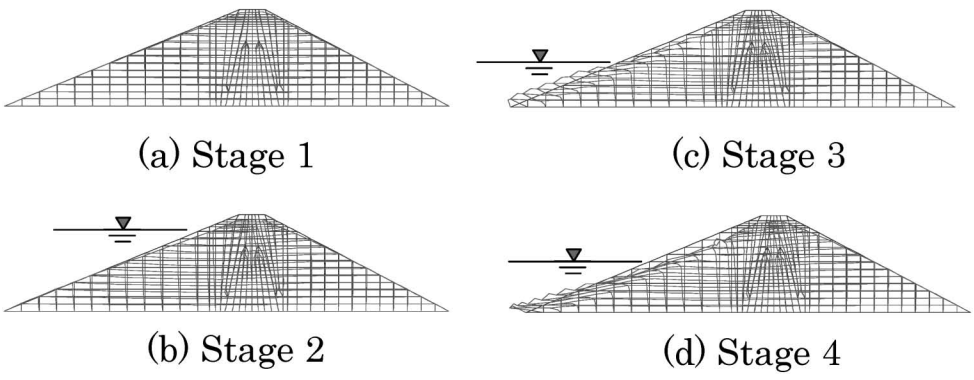


**Fig. 21. Deformations of the embankment during reservoir filling**

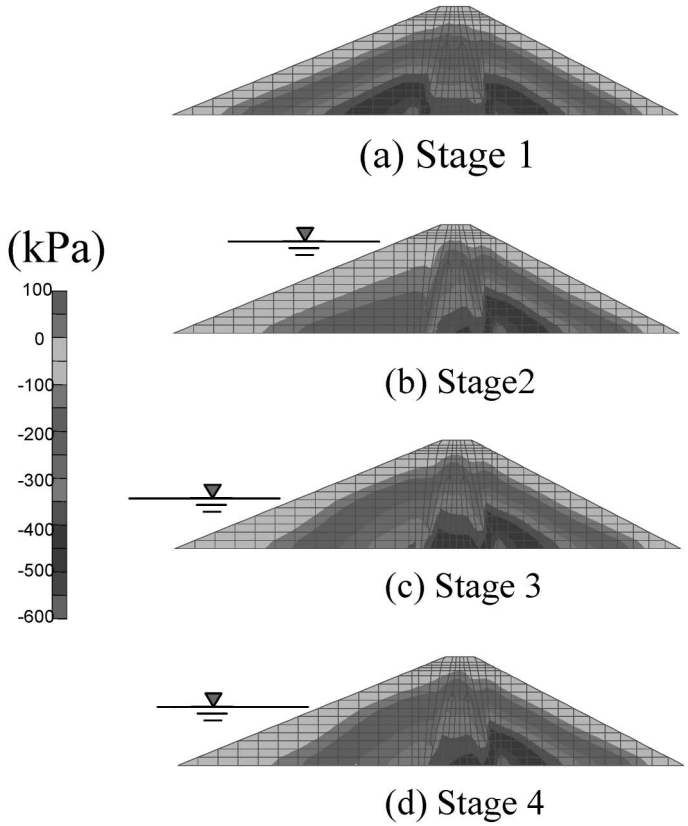


**Fig. 22. Vertical effective stress distributions within the embankment during reservoir filling**

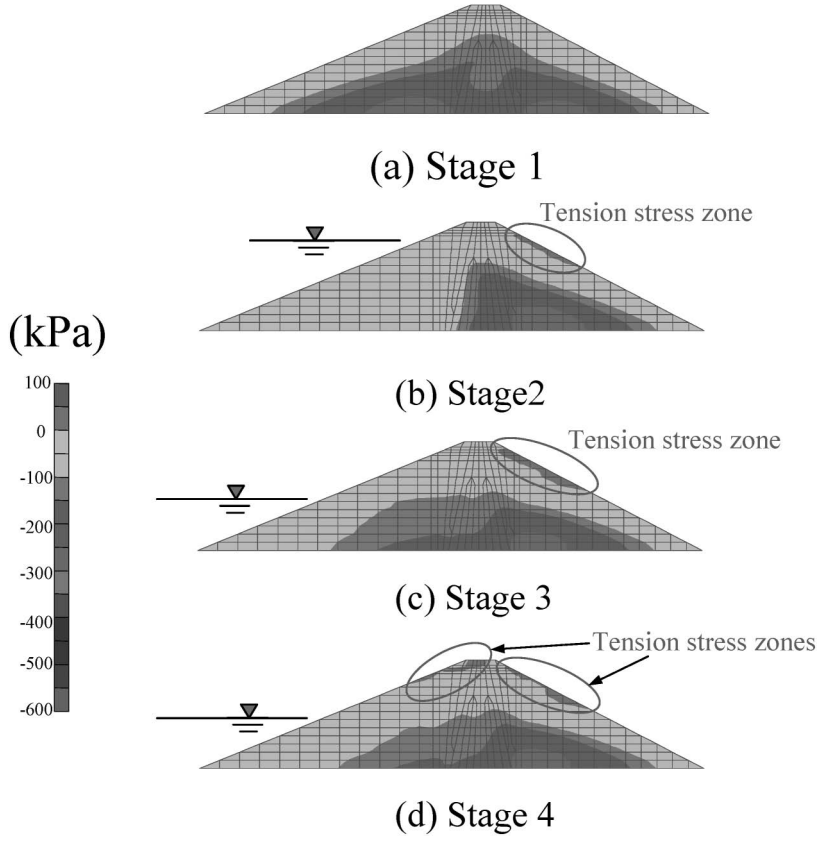


**Fig. 23. Horizontal effective stress distributions within the embankment during reservoir filling**

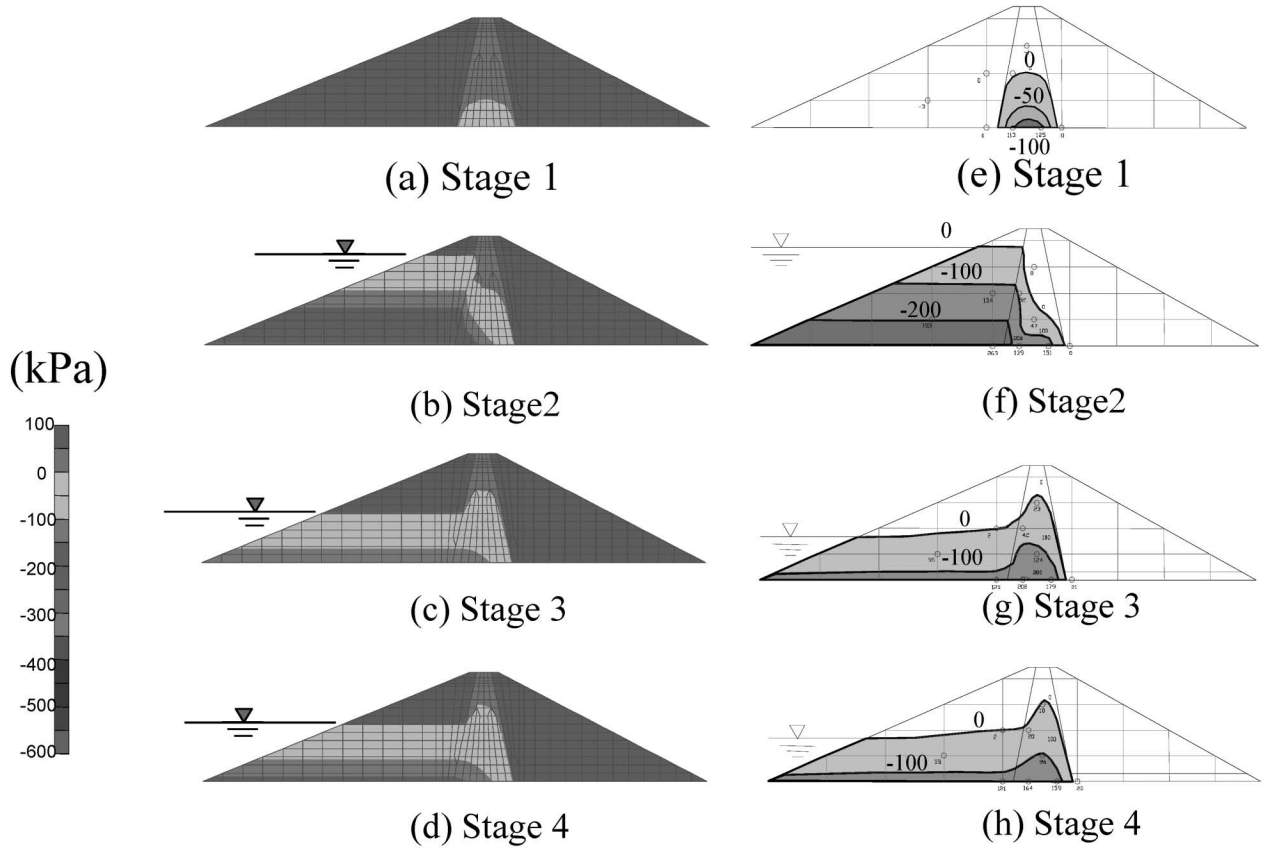


**Fig. 24. Pore water pressure distributions within the embankment during reservoir filling; Figs. (a)–(d): simulation results, Figs. (e)–(h): observed results**

per part of the downstream slope appeared as the water levels of the reservoir were going up (Stage 2). This is the reason why the embankment rotated toward upstream due to saturation collapse of the upstream rock material (*see* Fig. 23(b)). The tension zones expanded from the upper part of the downstream slope to the upper parts of the upstream slope through the crest of the embankment with the repeats of up-and-down water levels (Stages 3 and 4). Tension cracks may appear there. In this model test, such cracks were monitored after testing the places where tension stresses were calculated in the simulation (*see* Photo. 1).

Figure 24 shows the distributions of the pore water pressures calculated and measured. Figures 24(a)–(d) show the calculated results and Figs. 24(e)–(h) show the associated model test results. Comparing Figs. 24(a) and (e), the distribution patterns of pore water pressures within the core in both the experiment and simulation were convex upward and almost similar, but the values calculated were marginally smaller than those measured. In Stage 2, both distributions of the pore water pressures within the core zone showed an unsteady state. In Stages 3 and 4, which were associated with situations during drawing down of water levels, the residual pore water pressures could be seen within the core zone in both results. The values in the model test were larger than those in the simulation. Thus, the estimated pore water pressures within the core zone were marginally smaller than those measured at all the stages.

## CONCLUSION

We conducted a series of centrifuge model tests for a typical rockfill dam in order to investigate the behaviour of the dam due to cycles of reservoir water levels. The dam models consisted of comparatively well-compacted core zone and loosely compacted rock zone. We obtained the following main results from the model tests:

(1) Large amounts of settlements due to wetting within the upstream rock zone were monitored,
(2) The settlements increased when the reservoir water level went down and decreased when it rose up but the amounts were small and most of the settlements occurred during the first cycle of water levels,
(3) The crest of the dam at first moved upstream and then returned downstream during the first reservoir filling, and when reservoir water level went up the crest moved upstream and moved downstream when it went down,
(4) Cracks along the dam axis were observed on the upper parts of both upstream and downstream slopes.

We also tried to do a simulation of a typical result of the model tests by using the consolidation analysis method coupled with an elastoplastic model for unsaturated geo-materials. The main results obtained from the simulation are:

(1) The settlements calculated agreed mostly with those measured,
(2) The settlements due to wetting could be estimated within the upstream rock zone,
(3) The horizontal displacements upstream increased near the upstream slope with the cycles of up-and-down water levels and they concentrated to a shallow region near the upstream surface,
(4) Tension stresses were calculated at places where the cracks were monitored in the model test,
(5) Just after construction, arching actions in both the vertical and horizontal effective stress distributions could be seen on both the upstream and downstream boundaries between the core and rock zones but the arching actions on the upstream boundary disappeared with water levels going up.

Thus the simulation method presented an effective approach to analyze the behaviour of the fill-type dams during reservoir filling periods.

## ACKNOWLEDGMENTS

We would like to express our gratitude to Mr. Y. Sato (Obayashi-gumi) for his help and contribution towards this study.

## NOTATIONS

$\boldsymbol{B}$: nodal displacement-strain matrix
$\boldsymbol{B}_w$: gradient matrix for pore water pressure
$\boldsymbol{C}$: nodal displacement-volumetric strain matrix
$\boldsymbol{D}$: elastic matrix
$E'_f = E_f/n$ ($E_f = \partial S_r/\partial s$, $s$: suction, $n$: porosity)
$\boldsymbol{F}$: body force vector
$F_i$: components of body force vector
$G$: shear modulus
$J_2$: second deviator stress invariant
$K$: bulk modulus
$K_i$, $G_i$, $\gamma_J$ and $\gamma_p$: material parameters for elasticity
$N$: acceleration applied
$\boldsymbol{N}$: interpolation function for displacement
$\boldsymbol{N}_w$: interpolation function for pore water pressure
$\boldsymbol{Q}_b$: prescribed flux vector on the boundary nodal points
$\boldsymbol{R}$: permeability matrix
$S_{re}$: degree of saturation at air entry
$\boldsymbol{T}_b$: prescribed traction vector on the boundary nodal points
$a_e$: a material parameter for effective stress
$a_{st}$: change of storage of water due to change of degree of saturation
$\boldsymbol{a}_{st}$: vector of change of storage of water due to change of degree of saturation
$d_m$: model displacement
$d_p$: prototype displacement
$e_0$: initial void ratio
$k_s$: permeability at saturation
$m_p$ and $n_p$: material parameters for permeability
$p'$: mean effective stress
$p'_0$: initial mean effective stress
$\boldsymbol{q}$: flux vector
$q_i$: components of relative displacement velocity vector of water with respect to soil skeleton
$s$: suction
$s^*$: effective suction
$s^*_m$, $\lambda^*_{f1}$, $a^*_1$, $e^0_{01}$: material parameters for state surface
$s_e$: air entry suction
$t$: time
$t_m$: model time
$t_p$: prototype time
$\boldsymbol{u}$: nodal displacement vector
$u^*_i$: virtual displacement vector
$u_a$: pore air pressure
$u_{eq}$: equivalent pore pressure
$\boldsymbol{u}_w$: nodal pore water pressures
$u_w$: pore water pressure
$u^*_w$: virtual pore water pressure
$\Delta t$: increment of time
$\Delta \boldsymbol{u}$: increment of nodal displacement vector
$\Delta \boldsymbol{u}_w$: increment of nodal pore water pressures
$\Gamma^*_0$: initial value of $\Gamma^*$
$\Gamma^*$: void ratios of $e - \log(-p')$ curves in the elastoplastic range at $p' =$ unit
$\Gamma$: $\Gamma^*$ in saturation
$\alpha$: coefficient characterizing single-step temporal discretization
$R$: a material parameter with respect to the shape of the cap yield function
$\delta_{ij}$: Kronecker's delta
$\varepsilon_{ii}$: volumetric strain of soil skeleton
$\gamma$: unit weight of soil
$\phi'_{cs}$: friction angle at critical state
$\phi'$: friction angle at peak
$\kappa$: slope of $e - \log(-p')$ curve at unloading
$\lambda$: $\lambda^*$ in saturation
$\lambda^*_0$: initial value of $\lambda^*$
$\lambda^*$: slopes of $e - \log(-p')$ curves in the elastoplastic range
$\sigma$: total stress
$\sigma'$: effective stress
$\sigma'_{ij}$: effective stress tensor
$\boldsymbol{\sigma}'$: effective stress vector

## REFERENCES

1) Clough, R. W. and Woodward, R. J. (1967): Analysis of embankment stresses and deformations, *Proc.* ASCE 93, SM4, 529–549.
2) Fry, J. J., Charles, J. A. and Penman, A. D. (1995): Dams, embankments and slopes, *Proc. 1st Int. Conf. Unsaturated Soils*, Paris, Balkema, 1391–1419.
3) Ghaboussi, J. and Kim, K. J. (1986): Analysis of construction pore pressures in embankment dams, *Geomech. Modelling Eng. Practice* (eds. by Dungar, R. and Studer, J. A.), Balkema, 189–205.
4) Kohgo, Y. (2003): Review of constitutive models for unsaturated soils and initial-boundary value analyses, *Proc. 2nd Asian Conf. Unsaturated Soils*, Osaka, 21–40.
5) Kohgo, Y. (2008): A hysteresis model of soil water retention curves based on bounding surface concept, *Soils and Foundations*, **49**(5), 633–640.
6) Kohgo, Y., Asano, I. and Hayashida, Y. (2002): A numerical analysis method for static behavior of fill-type dams. *Proc. 3rd Int.*

*Conf. Dam Eng.*, Singapore, CI-Premier PTE LTD, 151–158.
7) Kohgo, Y., Asano, I. and Hayashida, Y. (2007): An elastoplastic model for unsaturated rockfills and its simulations of laboratory tests, *Soils and Foundations*, **47**(5), 919–929.
8) Kohgo, Y., Asano, I. and Tagashira, H. (2000): Application of FE consolidation analysis method to fill-type dams, *Proc. 1st Asian Conf. Unsaturated Soils*, Singapore, Balkema, 189–194.
9) Kohgo, Y., Nakano, M. and Miyazaki, T. (1993a): Theoretical aspects of constitutive modeling for unsaturated soils, *Soils and Foundations*, **33**(4), 49–63.
10) Kohgo, Y., Nakano, M. and Miyazaki, T. (1993b): Verification of the generalized elastoplastic model for unsaturated soils, *Soils and Foundations*, **33**(4), 64–73.
11) Kohgo, Y., Nakano, M. and Miyazaki, T. (1995): Closure—Verification of the generalized elastoplastic model for unsaturated soils, *Soils and Foundations*, **35**(1), 173–174.
12) Kohgo, Y., Takahashi, A., Asano, I. and Suzuki, T. (2006): FEM consolidation analysis of centrifuge test for rockfill dam model during first reservoir filling, *Unsaturated Soils 2006 Geotechnical Special Publication*, ASCE, **2**(147), 2312–2323.
13) Kohgo, Y. and Yamashita, T. (1988): Finite element analysis of fill type dams—Stability during construction by using the effective stress concept, *Proc. 6th Int. Conf. Numer. Methods Geomech.*, Innsbruck, Balkema, **2**, 1315–1322.
14) Laigle, F., Poulain, D. and Magnin, P. (1995): Numerical simulation of La Ganne dam behaviour by a three phases approach. *Proc. 1st Int. Conf. Unsaturated Soils*, Paris, Balkema, **1**, 315–320.
15) Nakagawa, K., Komada, H. and Kanazawa, K. (1985): Finite element analysis of pore pressure behavior, *Proc. 5th Int. Conf. Numer. Methods Geomech.*, Nagoya, Balkema, **2**, 919–926.
16) Ng, K. L. A. and Small, J. C. (1999): A case study of hydraulic fracturing using finite element methods, *Can. Geotech. J.*, **36**, 861–875.
17) Nobari, E. S. and Duncan, J. M. (1972): Effect of reservoir filling on stresses and movements in earth and rockfill dams, Report No. TE-72-1, University of California, Berkeley.
18) Pagano, L. and Desideri, A. (1998): Influence of water retention characteristic curve on dam behaviour during construction. *Proc. 2nd Int. Conf. Unsaturated Soils*, Beijin, 261–265.